

# A Bayesian Approach for Parameter Estimation and Prediction using a Computationally Intensive Model

Dave Higdon<sup>1</sup>, Jordan D McDonnell<sup>2</sup>, Nicolas Schunck<sup>2</sup>, Jason Sarich<sup>3</sup>, Stefan M Wild<sup>3</sup>

<sup>1</sup> Los Alamos National Laboratory, Statistical Sciences, Los Alamos, New Mexico 87545, USA

<sup>2</sup> Physics Division, Lawrence Livermore National Laboratory, Livermore, CA, 94551, USA

<sup>3</sup> Mathematics and Computer Science Division, Argonne National Laboratory, Argonne, IL 60439, USA

E-mail: dhigdon@lanl.gov

**Abstract.** Bayesian methods have been very successful in quantifying uncertainty in physics-based problems in parameter estimation and prediction [1, 2]. In these cases, physical measurements  $y$  are modeled as the best fit of a physics-based model  $\eta(\theta)$ , where  $\theta$  denotes the uncertain, best input setting. Hence the statistical model is of the form

$$y = \eta(\theta) + \epsilon,$$

where  $\epsilon$  accounts for measurement, and possibly other error sources. When non-linearity is present in  $\eta(\cdot)$ , the resulting posterior distribution for the unknown parameters in the Bayesian formulation is typically complex and non-standard, requiring computationally demanding computational approaches such as Markov chain Monte Carlo (MCMC) to produce multivariate draws from the posterior. While quite generally applicable, MCMC requires thousands, or even millions of evaluations of the physics model  $\eta(\cdot)$ . This is problematic if the model takes hours or days to evaluate. To overcome this computational bottleneck, we present an approach adapted from Bayesian model calibration [3]. This approach combines output from an ensemble of computational model runs with physical measurements, within a statistical formulation, to carry out inference. A key component of this approach is a statistical response surface, or emulator, estimated from the ensemble of model runs. We demonstrate this approach with a case study in estimating parameters for a density functional theory (DFT) model, using experimental mass/binding energy measurements from a collection of atomic nuclei. We also demonstrate how this approach produces uncertainties in predictions for recent mass measurements obtained at Argonne National Laboratory (ANL) [4].

PACS numbers: 21.10.-k, 21.30.Fe, 21.60.Jz, 21.65.Mn

## 1. Introduction

Bayesian calibration of computer models [3, 5, 6] combines output from an ensemble of computational model runs with physical measurements, within a statistical formulation, to carry out statistical and scientific inferences. These include quantifying the uncertainty in model parameters, as well as in model based predictions. Typically, because of the cost (both in time and computational resources) of evaluating the computational model, only a limited number of model evaluations can be made. Also, because the model can never exactly match the physical measurements, even at the best possible parameter input settings, the statistical formulation must account for this discrepancy.

Since the computational model cannot be quickly evaluated at any input setting when needed, an ensemble of model runs are carried out prior to the statistical analysis, producing the raw material from which to build a response surface, mapping the model parameter inputs to the model outputs of interest. A Gaussian process (GP) model is most commonly used to *emulate* the model response as a function of the inputs [7, 8]. Not only does the GP model typically produce an accurate emulator [9], it can also be embedded within a statistical formulation, allowing parameter estimation (calibration) and model-based prediction.

In this paper, we apply the Bayesian model calibration approach to the nuclear DFT model described in McDonnell et al. of this volume, as well as in other references [10, 11]. In order to streamline the presentation, we focus on nuclear masses for a number of spherical and deformed nuclei as the quantities of interest for both the model and the experimental measurements. The goal will be to estimate parameter uncertainties from this data, and to produce predictions, with uncertainty, for a recent set of mass measurements carried out at the CARIBU facility at Argonne National Laboratory [4].

In the following sections, we'll briefly review the experimental measurements and DFT model, and then go on to describe the statistical formulation in more detail. We'll apply the Bayesian model calibration approach to this data, producing updated uncertainties for the model parameters, and producing prediction uncertainties for the new ANL mass measurements, comparing the predictions to the actual measurements. We end with a discussion of this approach, pointing out features of this analysis, and describing strengths and weakness.

### 1.1. Bayesian Formulations

Before going into detail regarding the Bayesian formulation used for this case study, we give a brief overview of Bayesian approaches for parameter estimation, focusing on a simple, 1-d example shown in Figure 1. Physical data  $y$  is combined with a scientifically motivated model  $\eta(\cdot)$ . The model requires an input parameter  $\theta$  to make a prediction  $\hat{y} = \eta(\theta)$ . The goal is to use the data  $y$  to constrain uncertainty regarding  $\theta$ . Uncertainty in  $\theta$  then induces uncertainty on a new prediction  $\eta(\theta)$ .

The Bayesian paradigm requires specification of the likelihood  $L(y|\theta)$ , and the prior

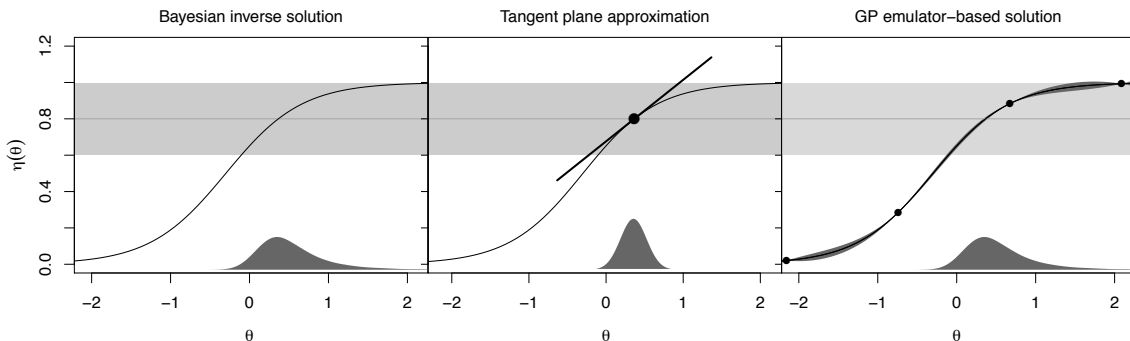


**Figure 1.** Possible Bayesian approximations to a 1-d estimation problem. The horizontal line represents the observation of  $y = .8$ , whose error has a standard deviation of  $\sigma = .1$ ; the  $\pm 2\sigma$  region is represented by the shaded region about the line. The sigmoid line shows the model  $\eta(\theta)$ , and the shaded density on the  $x$ -axis shows the posterior distribution for  $\theta$ . Left: the exact posterior density for  $\theta$  is estimated via MCMC; Middle: a linear tangent approximation to the model  $\eta(\cdot)$  is used to induce a normal approximation to the posterior density for  $\theta$ . Right: a GP is used to estimate  $\eta(\cdot)$ , producing a more accurate approximation to the posterior density for  $\theta$ .

for the unknown parameter  $\pi(\theta)$ . The inference is based on the posterior distribution, whose (unnormalized) density is just the product of the likelihood and the prior

$$\pi(\theta|y) \propto L(y|\theta) \times \pi(\theta).$$

In the simple example of Figure 1, the physical observation  $y$  is modeled as

$$y = \eta(\theta) + \epsilon, \text{ where } \epsilon \sim N(0, .1^2),$$

where  $\sim$  means “is distributed as.” Thus  $L(y|\theta) \propto \exp\{-\frac{1}{2} \cdot .1^{-2}(y - \eta(\theta))^2\}$ . For the prior we take  $\theta \sim N(0, 1)$  so that  $\pi(\theta) \propto \exp\{-\frac{1}{2}\theta^2\}$ . Thus the resulting posterior density for  $\theta$  is given by

$$\pi(\theta|y) \propto \exp\left\{-\frac{1}{2} \left[ .1^{-2}(y - \eta(\theta))^2 + \theta^2 \right]\right\}.$$

Bayesian inference requires understanding this resulting posterior distribution, and using it to make predictions for new observations  $y$ . While the 1-d example shown here is not too daunting, typical examples have a much higher-dimensional parameter space, including statistical nuisance parameters such as variances. In such cases, Markov chain Monte Carlo (MCMC) [12] can be used to draw samples from the posterior distribution. Typically, MCMC requires many thousands to millions of evaluations of the posterior. In our case study,  $\eta(\theta)$  represents a computationally demanding DFT model, making direct use of MCMC infeasible. A common alternative is to replace the computational model  $\eta(\theta)$  by a linear tangent model approximation. This linear assumption often results in overly narrow estimates of the parameter uncertainty (see the middle frame of Figure 1). In this paper we’ll develop a Gaussian process (GP) based approximation for  $\eta(\cdot)$ , allowing posterior sampling via MCMC.

## 1.2. DFT Model and Experimental Measurements

For this case study, the DFT model requires a  $p = 12$ -dimensional parameter vector  $t = (t_1, \dots, t_p)$  to produce fitted masses for any given nucleus. The parameters and their prior ranges are given in Table 1. For any input setting  $t$ , and any specified nucleus  $(N, Z)$ , the DFT code produces a fitted mass. Note that we use  $t$  to denote a generic setting of the inputs, reserving  $\theta$  to denote the unknown, best input setting, which is to be estimated from the experimental mass measurements.

**Table 1.** DFT model parameters and their prior ranges

parameter	label	$C_{\text{lower}}$	$C_{\text{upper}}$
$\rho_c$	$\theta_1$	0.155	0.165
$E^{NM}/A$	$\theta_2$	-16.0	-15.5
$K^{NM}$	$\theta_3$	200	240
$a_{\text{sym}}^{NM}$	$\theta_4$	27.0	31.0
$L_{\text{sym}}^{NM}$	$\theta_5$	15.0	65.0
$1/M_s^*$	$\theta_6$	0.75	1.25
$C_0^{\rho\Delta\rho}$	$\theta_7$	-60	-30
$C_1^{\rho\Delta\rho}$	$\theta_8$	-240	-50
$V_0^n$	$\theta_9$	-220	-150
$V_0^p$	$\theta_{10}$	-230	-180
$C_0^{\rho\nabla J}$	$\theta_{11}$	-90	-60
$C_1^{\rho\nabla J}$	$\theta_{12}$	-90	20

This example considers the masses of 28 spherical nuclei, 47 deformed nuclei, and 31 neutron rich nuclei, as shown in Figure 2. For a given input setting  $t$ , the DFT code is run to compute the masses for all  $n = n_1 + n_2 + n_3 = 28 + 47 + 31 = 105$  nuclei, producing an  $n$ -vector of outputs  $\eta(t)$ . For the Bayesian analysis, we generate an initial set of  $m = 183$  DFT model runs for each of these  $n$  nuclei. Note that the original design was for 200 parameter settings, but 17 of these runs were discarded due to convergence issues. The input settings used in this analysis are shown in Figure 3. The output range of the resulting  $n \times m = 19,215$  DFT runs are shown in Figure 2 for each of the 105 nuclei.

In addition to the model runs, each nuclei also has an experimentally determined mass denoted by the black dot in Figure 2. As a demonstration of this Bayesian model calibration methodology, we'll use the data from the 28 spherical and 47 deformed nuclei to constrain model parameter uncertainties, and to estimate model error. With these results, we compare the the resulting predictions, and their uncertainties, to the actual measurements of the 31 neutron rich nuclei recently measured at the CARIBU facility at ANL [4].

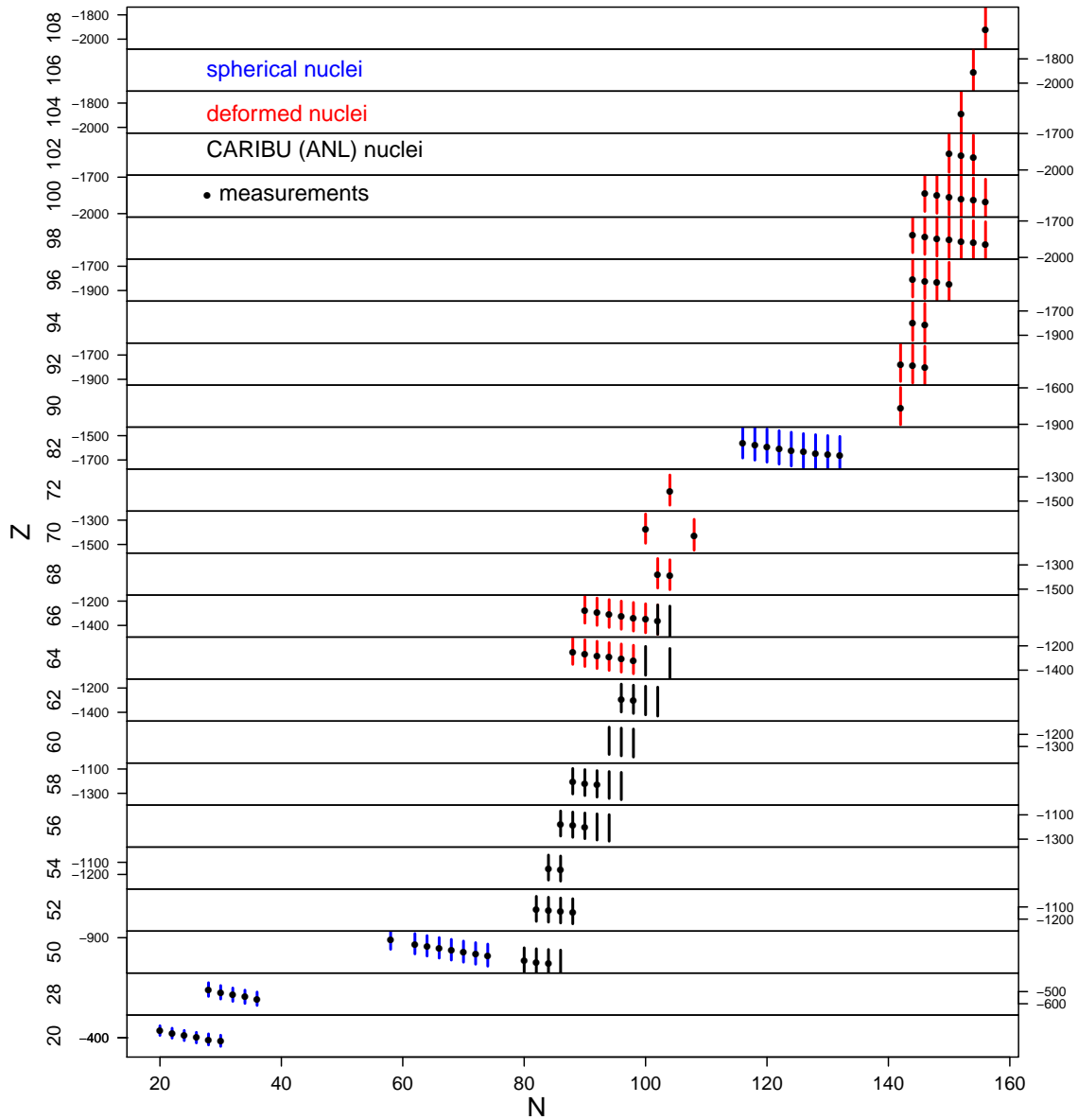


**Figure 2.** Range of DFT computed masses (vertical lines), along with the experimental measurements (dots) for 25 spherical (blue), 75 deformed (red), and newly measured neutron rich nuclei (black). The ranges of DFT computed masses are derived from the ensemble of 183 parameter settings shown in Figure 3.

## 2. Bayesian Formulation

The full Bayesian model formulation combines experimental measurements and an ensemble of DFT model runs, all within an encompassing statistical model. This encompassing model formulation is rather involved. Hence we describe its main components in the next three subsections. The first component, described in Section 2.1, is the GP model used to probabilistically describe the DFT output given parameter settings  $t$ . The second component, described in Section 2.3, is a full Bayesian model

calibration formulation for a single output type (spherical masses), using the simulation output, along with the experimental measurements to reduce parameter uncertainties. The third component combines separate formulations into a single Bayesian model, so that information from multiple data types can be used to estimate parameter uncertainties – both for the DFT model, as well as statistical parameters control the GP covariance and the error variance.

Once the various parameter uncertainties are estimated within this overarching statistical model, predictions and predictive distributions for outputs of interest can be determined. We'll compare the predictive distribution to each of the experimental measurements used for estimation (i.e. the masses for the spherical and deformed nuclei). We'll also compare predictive distributions for the new ANL mass measurements for neutron-rich nuclei. Since the ANL mass measurements were not used to estimate any of the model parameters, this will allow us to assess quality of the predictions produced by this statistical formulation.

### 2.1. Emulation of DFT Model Output

The DFT model requires between 5-10 minutes to compute the mass for a given nucleus. Given that the statistical analysis presented here involves 75 nuclei, requiring 75 DFT solves for every evaluation of  $\eta(\theta)$ , direct use of MCMC is not practical. In this case study, we opt to treat  $\eta(\cdot)$  as an unknown function, to be estimated from an initial set of  $m = 183$  DFT solves for each nucleus. In this section we describe a Bayesian approach for estimating  $\eta(\cdot)$  from the  $m$  training runs with a Gaussian process (GP) specification. A Bayesian approach is taken that can be integrated into the full model formulation described in following subsection.

The use of a GP model to *emulate* a computational model  $\eta(\cdot)$  at new parameter inputs dates back 25+ years [7, 13]. The approach has proven quite effective in a variety of applications where the model output changes smoothly as a function of the inputs  $\theta$  [14, 15, 16].

*2.1.1. The Ensemble of DFT Runs* We start with simulator runs at  $m$  different input settings

$$\eta(t_j^*), \quad j = 1, \dots, m.$$

We use a space-filling Latin hypercube [17] sample for this initial design of input settings  $(t_1^*, \dots, t_m^*)$ . We use  $\mathbf{t}^*$  to denote the  $m \times p$  matrix describing this design, or ensemble of input settings. Two-dimensional projections of this parameter design are shown in Figure 3. How best to construct a design for an emulator is still a research topic in the statistical literature; a starting point to this literature can be found in Santer et al.'s textbook [18] and the references therein.

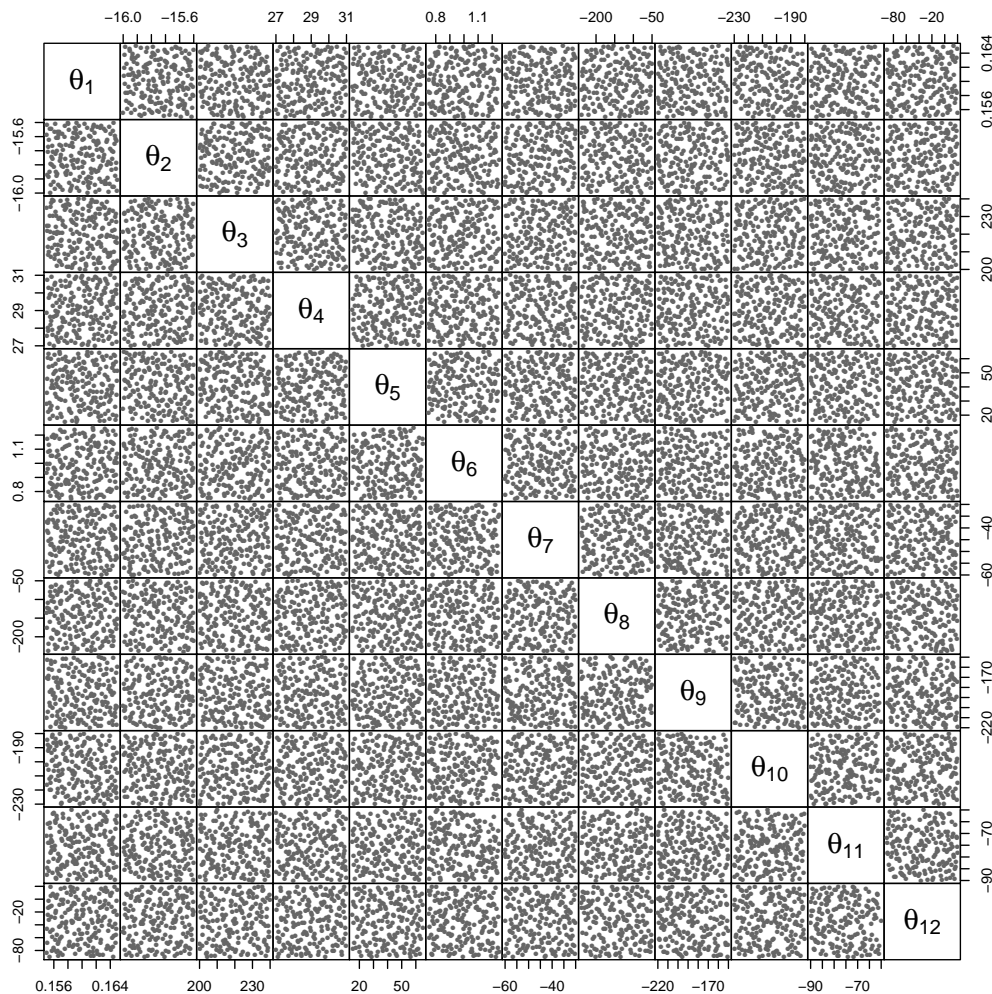


**Figure 3.** The space-filling Latin hypercube sample (LHS) used to specify the initial set of DFT runs with which to construct the GP emulator. The 2-d projections of this design are shown for each pair of parameters.

## 2.2. Basis Representation of the DFT Model Output

We focus on a single output type in this subsection – the  $n = 28$  masses for the spherical nuclei. Also, to simplify the model specification, we standardize the  $p = 12$ -dimensional parameter space to  $C = [0, 1]^p$  using the ranges given in Table 1. For a given input  $t$  in the standardized input space  $[0, 1]^p$ , the DFT model produces an  $n$ -vector  $\eta(t)$ , giving the mass for each of the  $n$  nuclei. The emulator models the DFT output using a  $q$ -dimensional basis representation:

$$\eta(t) = \sum_{i=1}^q \phi_i w_i(t) + e, \quad t \in [0, 1]^p, \quad (1)$$

where  $\{\phi_1, \dots, \phi_q\}$  are orthogonal,  $n$ -dimensional basis vectors, the  $w_i(t)$  are weights whose value depends on  $t$ , and  $e$  is an  $n$ -dimensional error term, accounting for the

residual in the basis representation, as well as numerical noise from the DFT code. This formulation builds an emulator that maps  $[0, 1]^p$  to  $R^n$  by building  $q$  independent, univariate models for each  $w_i(t)$ . Separate Gaussian processes models [7, 19] are used to model each of the weight functions.

For each of the  $m = 183$  settings  $(t_1^*, \dots, t_m^*)$  of parameter design, an  $n$ -dimensional vector of masses is produced, giving  $\eta_1, \dots, \eta_m$ . These output vectors are represented via principal components [20], or, equivalently, empirical orthogonal functions (EOFs) [21]. Following standard practice, the output vectors are centered by subtracting the mean  $(\frac{1}{m} \sum_{j=1}^m \eta_j)$  from each output vector. Alternative standardizations may be preferred, depending on the application. This same standardization is also applied to the experimental data.

We obtain the  $n \times m$  matrix  $\Xi$  by column-binding the (standardized) output vectors from the simulations. Applying the singular value decomposition (SVD) to the simulation output matrix  $\Xi$  gives

$$\Xi = [\eta_1; \dots; \eta_m] = UDV', \quad (2)$$

where  $U$  is a  $n \times m$  orthogonal matrix,  $D$  is a diagonal  $m \times m$  matrix holding the singular values, and  $V$  is a  $m \times m$  orthonormal matrix. To construct a  $q$ -dimensional representation of the simulation output, we define the EOF basis matrix  $\Phi_\eta$  to be the first  $q$  columns of  $[UD\sqrt{m}]$ . We take  $q = 9$ ; this is sufficient to explain over 99.9% of the variation in the simulation ensemble. For illustration, the first three basis functions  $\phi_1, \dots, \phi_3$  are shown in Figure 4. Note that the  $\phi_i$  are  $n = 27$ -vectors, with one element for each spherical nucleus.

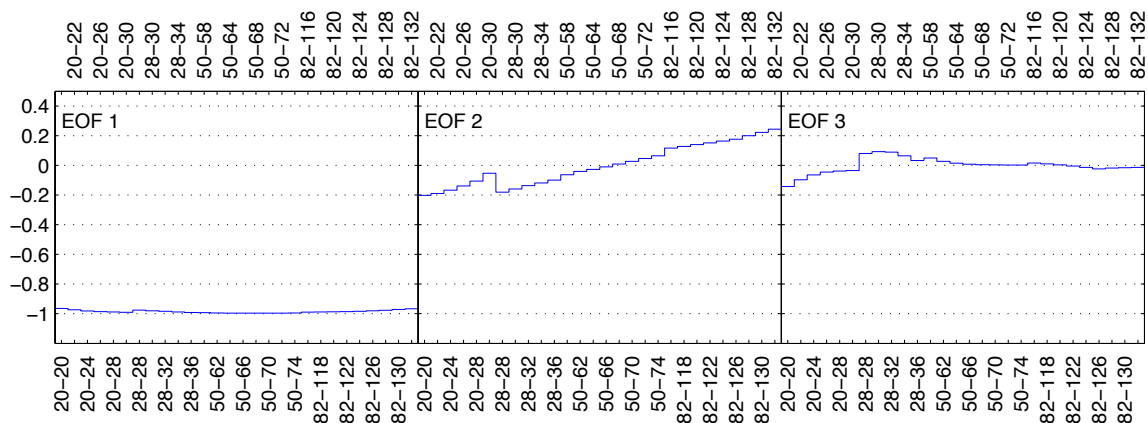


**Figure 4.** The first three basis functions  $\phi_i$ ,  $i = 1, \dots, 3$ , over each of the 28 spherical nuclei. Here each of the basis functions are derived using empirical orthogonal functions from the 183 simulations. Each nucleus is labeled  $Z$ - $N$ .

*2.2.1. Specifying the Gaussian Process Model Emulator* Each of the basis weights in Equation (1),  $w_i(t)$ ,  $i = 1, \dots, q$ , is a function mapping the  $p$ -dimensional input  $t$  to a



scalar. These functions are modeled (a priori) as independent, zero mean GP's.

$$w_i(\cdot) \sim \text{GP}(\mu(\cdot), C(\cdot, \cdot)) \text{ with } \mu(t) = 0, C(t, t') = \lambda_{w_i}^{-1} R(t, t'; \rho_i), \quad (3)$$

where  $\lambda_{w_i}$  is the marginal precision of the process and  $R(t, t'; \rho_i)$  is a correlation function, whose entries depend on the pair of input settings  $t$  and  $t'$ , as well as the vector  $\rho_i = (\rho_{i1}, \dots, \rho_{ip})'$

$$R(t, t'; \rho_i) = \prod_{k=1}^p \rho_{ik}^{4(t_k - t'_k)^2}. \quad (4)$$

This is the Gaussian covariance function, giving very smooth realizations, and commonly used to model computer simulation output [3, 7]. This fits well with our expectation that the DFT masses will change smoothly as the input values are changed. An advantage of the product form is that only a single additional parameter is required per additional input dimension, while the fitted GP response still allows for rather general interactions between inputs. The parameter  $\rho_{ik}$  controls the spatial range for the  $k$ th input dimension of the process  $w_i(\cdot)$ . Under this parameterization,  $\rho_{ik}$  gives the correlation between  $w_i(t)$  and  $w_i(t')$  when the input conditions  $t$  and  $t'$  are identical, except for a difference of 0.5 in the  $k$ th component. Note that this interpretation makes use of the standardization of the input space to  $[0, 1]^p$ .

Restricting to the  $m$  input design settings, we define the  $m$ -vector  $w_i$  to be  $w_i = (w_i(t_1^*), \dots, w_i(t_m^*))'$  for  $i = 1, \dots, q$ . In addition we define  $R(\mathbf{t}^*; \rho_i)$  to be the  $m \times m$  correlation matrix resulting from applying equation (4) to each pair of input settings in the design  $\mathbf{t}^*$ . The  $p$ -vector  $\rho_i$  gives the correlation distances for each of the input dimensions. At the  $m$  simulation input settings, the  $mq$ -vector  $w = (w'_1, \dots, w'_q)'$  then has prior distribution

$$\begin{pmatrix} w_1 \\ \vdots \\ w_q \end{pmatrix} \sim N \left( \begin{pmatrix} 0 \\ \vdots \\ 0 \end{pmatrix}, \begin{pmatrix} \lambda_{w_1}^{-1} R(\mathbf{t}^*; \rho_1) & 0 & 0 \\ 0 & \ddots & 0 \\ 0 & 0 & \lambda_{w_q}^{-1} R(\mathbf{t}^*; \rho_q) \end{pmatrix} \right), \quad (5)$$

which is controlled by  $q$  precision parameters held in  $\lambda_w$  and  $q \cdot p$  spatial correlation parameters held in  $\rho$ . The prior above can be written more compactly as  $w \sim N(0, \Sigma_w)$ , where  $\Sigma_w$ , controlled by parameter vectors  $\lambda_w$  and  $\rho$ , is given by the block diagonal covariance matrix in equation (5).

*2.2.2. Bayesian Representation of the GP Emulator* We specify independent Gamma priors  $Ga(a_w, b_w)$  for each  $\lambda_{w_i}$  and independent Beta priors for the  $\rho_{ik}$ , giving the prior densities

$$\begin{aligned} \pi(\lambda_{w_i}) &\propto \lambda_{w_i}^{a_w - 1} e^{-b_w \lambda_{w_i}}, \quad i = 1, \dots, q, \\ \pi(\rho_{ik}) &\propto \rho_{ik}^{a_\rho - 1} (1 - \rho_{ik})^{b_\rho - 1}, \quad i = 1, \dots, q, k = 1, \dots, p. \end{aligned} \quad (6)$$

We expect the marginal variance for each  $w_i(\cdot)$  process to be close to one due to the scaling of the basis functions. For this reason we specify that  $a_w = b_w = 5$ ,

encouraging each  $\lambda_{wi}$  to be close to 1. In addition, this informative prior helps stabilize the resulting posterior distribution for the correlation parameters which can trade off with the marginal precision parameter. Because we expect only a subset of the inputs to influence the simulator response, our prior for the correlation parameters reflects this expectation of *effect sparsity*. Under the parameterization in equation (4), input  $k$  is inactive for PC  $i$  if  $\rho_{ik} = 1$ . Choosing  $a_\rho = 1$  and  $0 < b_\rho < 1$  will give a density with substantial prior mass near one. We take  $b_\rho = 0.1$ , which makes  $\Pr(\rho_{ik} < 0.98) \approx \frac{1}{3}$  a priori. In general, the selection of these hyperparameters should depend on how many of the  $p$  inputs are expected to be active.

We can now define the likelihood, or sampling model, for the simulation output  $\eta$ . Here  $\eta = \text{vec}(\Xi)$ , where  $\text{vec}(\Xi)$  produces a vector by stacking the columns of matrix  $\Xi$ . Taking the error vector in Equation (1) to be independent Gaussian with common precision  $\lambda_\eta$ , we get the sampling model, or likelihood, for  $\eta$ :

$$\eta|w, \lambda_\eta \sim N(\Phi w, \lambda_\eta^{-1} I), \quad (7)$$

where  $\Phi = [I_m \otimes \phi_1; \dots; I_m \otimes \phi_q]$ , and the  $\phi_i$  are the  $q$  basis vectors previously computed via SVD. A  $Ga(a_\eta, b_\eta)$  is specified for the error precision  $\lambda_\eta$ .

Multiplying the probability density functions implied by Equations (5), (6), and (7) and the Gamma prior for  $\lambda_\eta$  yields the (unnormalized) posterior density. After integrating out  $w$ , the posterior distribution for the unknown parameters becomes

$$\begin{aligned} \pi(\lambda_\eta, \lambda_w, \rho|\eta) \propto & \\ & |(\lambda_\eta \Phi' \Phi)^{-1} + \Sigma_w|^{-\frac{1}{2}} \exp\{-\frac{1}{2} \hat{w}' ((\lambda_\eta \Phi' \Phi)^{-1} + \Sigma_w)^{-1} \hat{w}\} \times \\ & \lambda_\eta^{a_\eta^* - 1} e^{-b_\eta^* \lambda_\eta} \times \prod_{i=1}^q \lambda_{wi}^{a_w - 1} e^{-b_w \lambda_{wi}} \times \prod_{i=1}^q \prod_{j=1}^p (1 - \rho_{ij})^{b_\rho - 1}, \end{aligned} \quad (8)$$

where

$$\begin{aligned} a_\eta^* &= a_\eta + \frac{m(n-q)}{2}, \\ b_\eta^* &= b_\eta + \frac{1}{2} \eta' (I - \Phi (\Phi' \Phi)^{-1} \Phi') \eta, \text{ and} \\ \hat{w} &= (\Phi' \Phi)^{-1} \Phi' \eta. \end{aligned} \quad (9)$$

In some applications  $\hat{w}$  – the simulation output dotted with the basis vectors – may not exactly conform to a smooth response over the input space. This is often due to numerical jitter in the computational model. In such cases, an additional error may be required. We typically add the  $m q \times m q$  covariance matrix  $\text{diag}(\lambda_{o1} I_m, \dots, \lambda_{oq} I_m)$  to the covariance term in (8) allow for some mismatch between  $\hat{w}_i$  and  $w(t_i)$ . In this case independent,  $Ga(1, .0001)$  priors are used for the  $\lambda_{oi}$ 's.

*2.2.3. Exploring the Posterior Distribution for the Emulator* This posterior distribution is a necessary ingredient for the complete formulation that incorporates the experimental data. However, it is worth exploring this intermediate posterior distribution for the DFT model response. It can be explored via MCMC using standard

Metropolis updates [22, 12] and we can view a number of posterior quantities to illuminate features of the DFT model. The posterior of the emulator response can be used to investigate sensitivity measures of computational model [8], or estimate a Sobol decomposition of the model response [7]. Figure 5 shows boxplots of the posterior distributions for the components of  $\rho$ . From this figure it is apparent that the PC's are influenced by a number of the components in  $t$ . Figure 6 shows the resulting posterior mean surfaces for  $w_1(\cdot)$ ,  $w_2(\cdot)$  and  $w_3(\cdot)$  as a function of  $t_6$  and  $t_7$ .

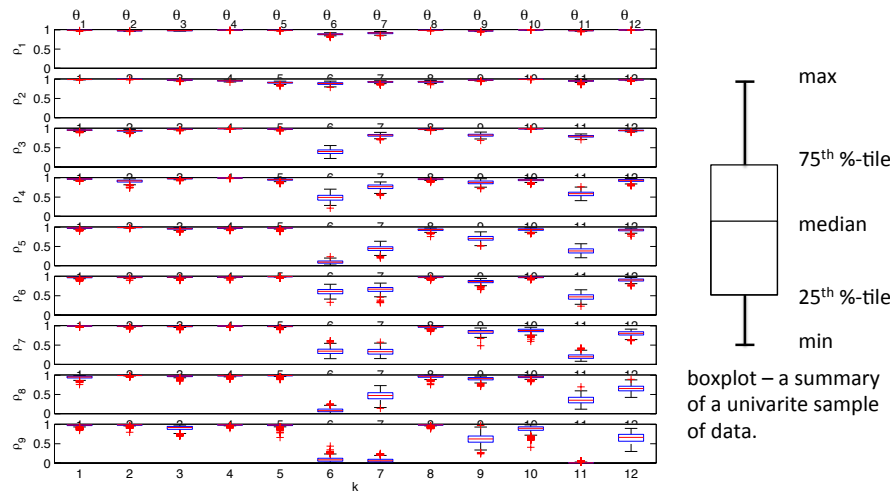


**Figure 5.** Boxplots of posterior samples for each  $\rho_{ik}$ , which control the GP response surface that predicts mass for the spherical nuclei as a function of the 12 DFT parameters.

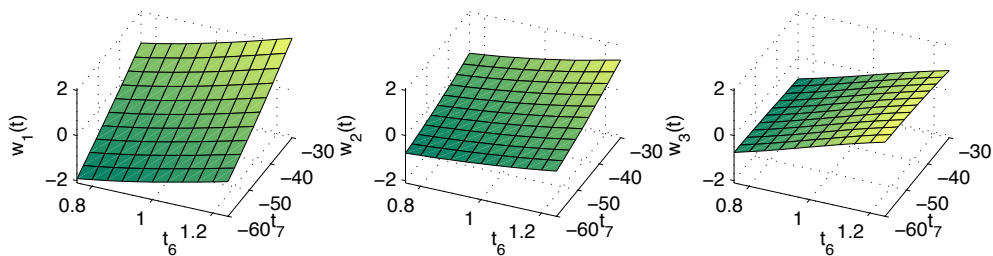


**Figure 6.** Posterior mean surfaces for  $w_i(\cdot)$ ,  $i = 1, 2, 3$ , the weights corresponding to the first three EOF's. Here the remaining 10 parameters were held at their midpoints as  $t_6$  and  $t_7$  vary over their design range.

**2.2.4. Generating Emulator-based Predictions** Given the posterior realizations from Equation (8), one can generate realizations from the process  $\eta(\cdot)$  at any input setting  $t^*$ . Since

$$\eta(t^*) = \sum_{i=1}^q \phi_i w_i(t^*), \tag{10}$$

realizations from the  $w_i(t^*)$  processes need to be drawn given the MCMC output. For a given draw  $(\lambda_\eta, \lambda_w, \rho)$  a draw of  $w^* = (w_1(t^*), \dots, w_q(t^*))'$  can be produced by using the fact

$$\begin{pmatrix} \hat{w} \\ w^* \end{pmatrix} \sim N \left( \begin{pmatrix} 0 \\ 0 \end{pmatrix}, \left[ \begin{pmatrix} (\lambda_\eta \Phi' \Phi)^{-1} & 0 \\ 0 & 0 \end{pmatrix} + \Sigma_{w, w^*}(\lambda_w, \rho) \right] \right), \quad (11)$$

where  $\Sigma_{w, w^*}$  is obtained by applying the covariance rule from Equation (4) to the augmented input settings that include the original design  $\mathbf{t}$  and the new input setting  $t^*$ . Recall that  $\hat{w} = (\Phi' \Phi)^{-1} \Phi' \eta$ . Application of the conditional normal rules then gives

$$w^* | \hat{w} \sim N(V_{21} V_{11}^{-1} \hat{w}, V_{22} - V_{21} V_{11}^{-1} V_{12}), \quad (12)$$

where

$$V = \begin{pmatrix} V_{11} & V_{12} \\ V_{21} & V_{22} \end{pmatrix} = \left[ \begin{pmatrix} (\lambda_\eta \Phi' \Phi)^{-1} & 0 \\ 0 & 0 \end{pmatrix} + \Sigma_{w, w^*}(\lambda_w, \rho) \right] \quad (13)$$

is a function of the parameters produced by the MCMC output. Hence, for each posterior realization of  $(\lambda_\eta, \lambda_w, \rho)$ , a realization of  $w^*$  can be produced. The above recipe easily generalizes to give predictions over many input settings at once.

Figure 7 shows posterior means for the simulator response  $\eta(\cdot)$  where each of the inputs is varied over its prior (standardized) range of  $[0, 1]$  while the other 11 inputs are held at their midpoints.

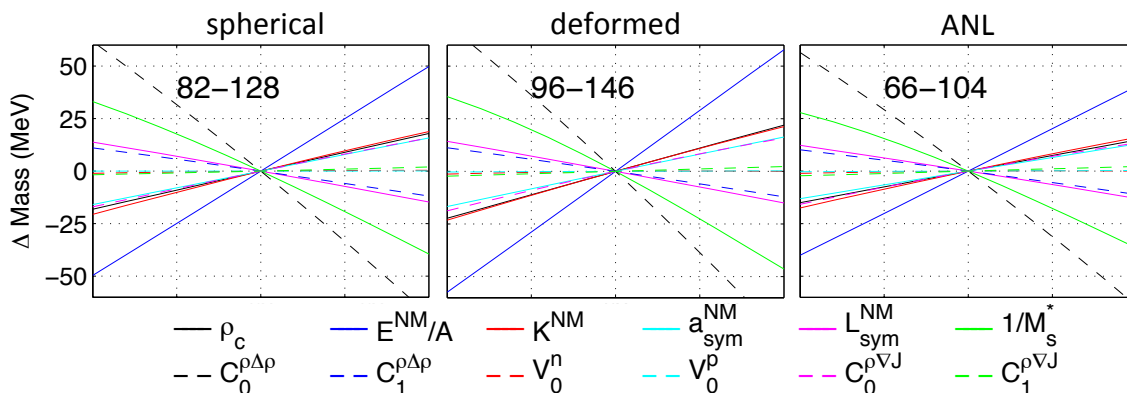


**Figure 7.** Sensitivity of the masses computed via DFT as each of the 12 parameters are varied from low to high (for ranges see table 1). The plots show how computed masses change for three different nuclei (Z-N) – one spherical, one deformed, and one from the new ANL measurements – as the parameters are varied, one at a time.

The posterior mean response conveys an idea of how the different parameters affect the computed masses for these three nuclei. The sensitivities for other spherical, deformed, and neutron-rich ANL masses are very similar. Other marginal functionals of the simulation response can also be calculated such as sensitivity indices or estimates of the Sobol decomposition [7, 8]. Note that a simpler emulator could have been constructed by estimating  $(\lambda_\eta, \lambda_w, \rho)$  via the posterior mean, or via maximum likelihood. Conditional on these parameters, the model output could be emulated using the mean in equation (12).

### 2.3. Full Bayesian GP-based Formulation – Single Output Type

We now describe the model formulation that incorporates experimental measurements to constrain uncertainty regarding the DFT parameter vector  $\theta$ . We first focus on a the spherical mass data and emulator; in the following section, we describe how the multiple data types can be combined in a common formulation. Hence we'll use  $n$  to denote the number of experimental measurements,  $m$  to denote the number of model runs for each nucleus,  $(\lambda_y, \lambda_\eta, \lambda_w, \rho)$  to denote the model parameters specific to this data type, leaving the distinction between data types to be made in the following subsection.

We have mass measurements for  $n = 28$  spherical nuclei held in the  $n$ -vector  $y$ . While these measurements are very accurate, we expect errors  $\epsilon$  between the measurements and the DFT code, even at the (unknown) best setting  $\theta$ , giving

$$y = \eta(\theta) + \epsilon,$$

where the errors are modeled as  $N(0, \Sigma_y)$ . We define  $\Sigma_y = \lambda_y^{-1} I_n$ , and specify a diffuse  $Ga(a_y = 1, b_y = .005)$  prior for  $\lambda_y$ , allowing the experimental measurements to inform about these precisions. Using the basis representation for  $\eta(\cdot)$  in (1), this results in a normal-gamma form for the data model

$$y|w(\theta), \lambda_y \sim N(\Phi w(\theta), \Sigma_y), \quad \lambda_y \sim Ga(a_y, b_y). \quad (14)$$

We can now write out the entire posterior distribution for all of the parameters, including  $\theta$ . First, let

$$\begin{aligned} \hat{w}_y &= (\Phi' \Sigma_y^{-1} \Phi)^{-1} \Phi' \Sigma_y^{-1} y, \\ a_y^* &= a_y + \frac{1}{2}(n - q), \\ W_y &= \lambda_y I_n, \\ b_y^* &= b_y + \frac{1}{2}(y - \Phi \hat{w}_y)' W_y (y - \Phi \hat{w}_y), \\ \Lambda_y &= \Phi' \Sigma_y^{-1} \Phi, \\ \Lambda_\eta &= \lambda_\eta \Phi' \Phi, \\ \Sigma_{w_y} &= \text{diag}(\lambda_{w_1}^{-1}, \dots, \lambda_{w_q}^{-1}), \\ \Sigma_{w_y w} &= \begin{pmatrix} \lambda_{w_1}^{-1} R(\theta, \mathbf{t}^*; \rho_1) & 0 & 0 \\ 0 & \ddots & 0 \\ 0 & 0 & \lambda_{w_q}^{-1} R(\theta, \mathbf{t}^*; \rho_q) \end{pmatrix}, \end{aligned} \quad (15)$$

where  $R(\theta, \mathbf{t}^*; \rho)$  is the  $1 \times m$  matrix with elements  $R(\theta, t_j^*; \rho)$ ,

$$\begin{aligned} \hat{z} &= \begin{pmatrix} \hat{w}_y \\ \hat{w} \end{pmatrix}, \\ \Sigma_{\hat{z}} &= \begin{pmatrix} \Lambda_y^{-1} & 0 \\ 0 & \Lambda_\eta^{-1} \end{pmatrix} + \begin{pmatrix} \Sigma_{w_y} & \Sigma_{w_y w} \\ \Sigma'_{w_y w} & \Sigma_w \end{pmatrix}. \end{aligned}$$

The posterior distribution has the form

$$\begin{aligned} \pi(\lambda_\eta, \lambda_w, \rho, \lambda_y, \theta | \hat{z}) \propto & \\ |\Sigma_{\hat{z}}|^{-\frac{1}{2}} \exp \left\{ -\frac{1}{2} \hat{z}' \Sigma_{\hat{z}}^{-1} \hat{z} \right\} \times \lambda_\eta^{\alpha_\eta^* - 1} e^{-b_\eta^* \lambda_\eta} \times \prod_{i=1}^q \lambda_{wi}^{a_w - 1} e^{-b_w \lambda_{wi}} \times & \quad (16) \\ \prod_{i=1}^q \prod_{k=1}^p \rho_{ik}^{\alpha_\rho - 1} (1 - \rho_{ik})^{b_\rho - 1} \times \prod_{i=1}^2 \lambda_{yi}^{\alpha_y^* - 1} e^{-b_y^* \lambda_{yi}} \times I[\theta \in C], & \end{aligned}$$

where  $C$  denotes the 12-dimensional rectangle given in Table 1 and shown in Figure 3.

#### 2.4. Full Bayesian GP-based Formulation – Combining Multiple Output Types

The posterior density in (16) captures the parameter uncertainty resulting from combining the spherical mass measurements with our statistical model formulation. This posterior has the general form

$$\{L(\hat{z} | \lambda_\eta, \lambda_w, \rho, \lambda_y, \theta) \cdot \pi(\lambda_\eta) \cdot \pi(\lambda_w) \cdot \pi(\rho) \cdot \pi(\lambda_y)\} \cdot \pi(\theta)$$

where the terms within the braces are specific to this particular data type. We can derive similar posteriors for additional data types. These multiple data types can be combined to inform about  $\theta$  by producting up the terms within the brackets for each data type. Hence information from  $K$  data types could be combined with the posterior below

$$\prod_{k=1}^K \{L(\hat{z}^{(k)} | \lambda_\eta^{(k)}, \lambda_w^{(k)}, \rho^{(k)}, \lambda_y^{(k)}, \theta) \cdot \pi(\lambda_\eta^{(k)}) \cdot \pi(\lambda_w^{(k)}) \cdot \pi(\rho^{(k)}) \cdot \pi(\lambda_y^{(k)})\} \cdot \pi(\theta) \quad (17)$$

where the superscript  $(k)$  indexes the data type. This product form assumes independence between error terms from different data sources.

Realizations from the posterior distribution (17) are produced using standard, single site MCMC. Metropolis updates [23] are used for the components of  $\rho$  and  $\theta$  with a uniform proposal distribution centered at the current value of the parameter. The precision parameters  $\lambda_\eta$ ,  $\lambda_w$  and  $\lambda_y$  are sampled using Hastings updates [24]. Here the proposals are uniform draws, centered at the current parameter values, with a width that is proportional to the current parameter value. We tune the candidate proposal width for good Monte Carlo efficiency.

### 3. Posterior Results

The resulting posterior distribution estimate for  $\theta$  is shown in Figure 8 on the original scale. The posterior values can also be propagated through the emulator to produce realizations of the model predictions. All of the predictions are centered at the nominal DFT prediction using the parameter setting  $t^0$  given in [25]. Thus the figures show the difference: prediction –  $\eta(t^0)$ . Figure 9 shows 90% prediction intervals for masses of the

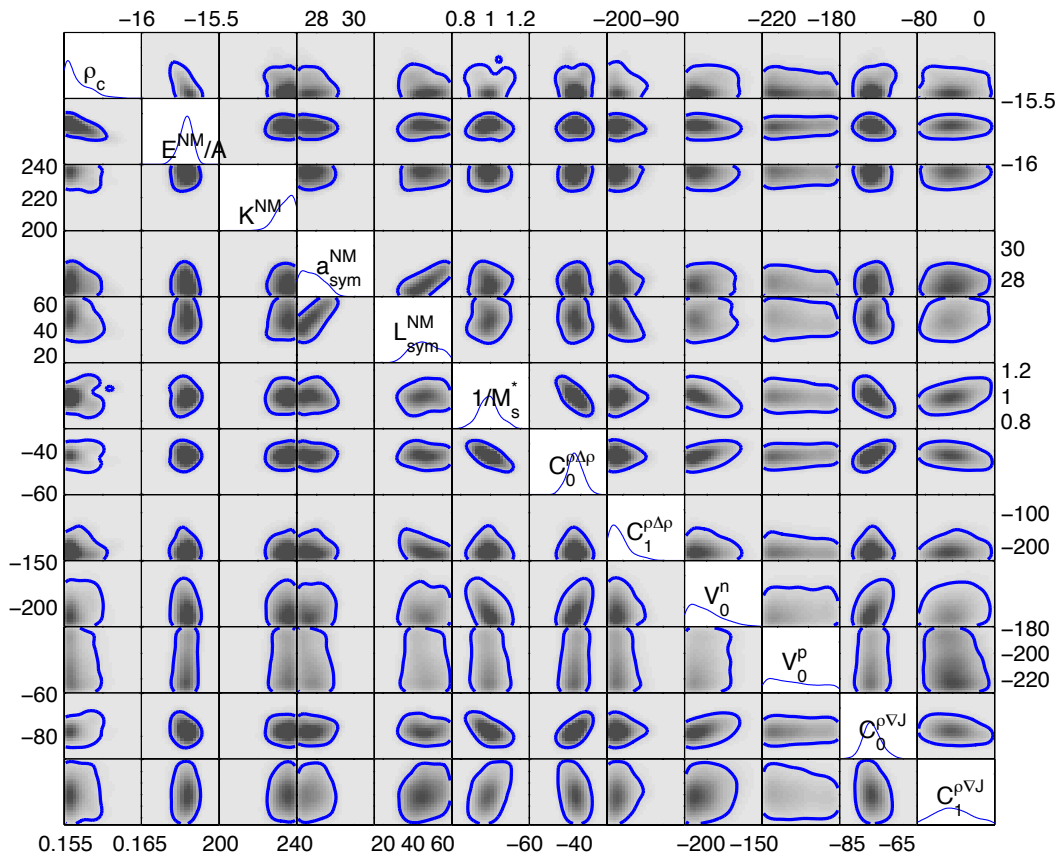


**Figure 8.** Univariate and bivariate marginal estimates of the posterior distribution for the 12-dimensional DFT parameter vector  $\theta$ , conditioning on mass measurements from the spherical and deformed nuclei. The blue line encloses an estimated 95% region.

spherical and deformed nuclei used in this formulation. The dark blue bands show 90% intervals for  $\eta(\theta)$  – the result of propagating uncertainty in  $\theta$  through the emulator, along with uncertainty in the emulator. The light blue bands show 90% prediction intervals for the actual measured value  $\eta(\theta) + \epsilon$ . This prediction also includes the effect of uncertainty in  $\epsilon$  – the error between  $\eta(\theta)$  and  $y$ . The magnitude of these errors is controlled by  $\lambda_y$ , which differs for the two data types.

Comparing the posterior predictions, along with their uncertainty, with the actual mass measurements gives an idea of how well the statistical formulation models the experimental measurements. The mass predictions are more accurate for the deformed nuclei. The dark blue parameter uncertainty bands for  $\eta(\theta)$  contain all of the experimental measurements, and the estimated standard deviation of  $\epsilon$  is about 0.8 MeV. For the spherical nuclei, 7 of the 28 measurements are not contained in the 90% prediction bands for  $\eta(\theta)$ , and the estimated standard deviation of  $\epsilon$  is about 1.3 MeV. This larger standard deviation for  $\epsilon$  is required to make the experimental measurements of spherical nuclei compatible with the statistical model formulation. This difference in prediction quality is primarily because the DFT model more accurately predicts the experimentally measured masses for deformed nuclei.

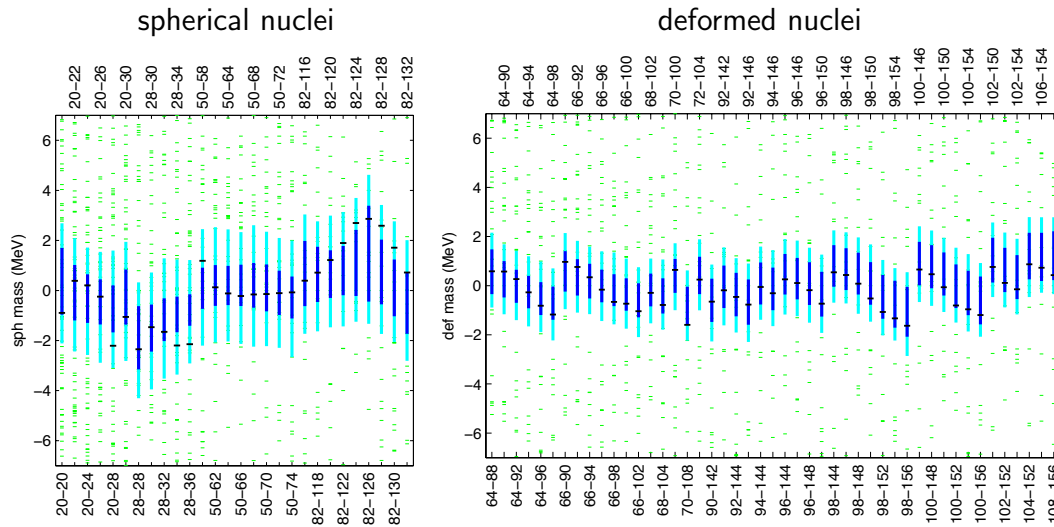


**Figure 9.** Posterior predictions for the masses of the spherical and deformed nuclei. The blue intervals correspond to  $\eta(\theta)$ ; the light blue intervals correspond to  $\eta(\theta) + \epsilon$ . DFT model output is represented by the green dashes, and experimental measurements by the black dashes. Each nucleus is labeled Z-N.

### 3.1. Prediction of ANL Mass Measurements

Using the posterior distribution resulting from this analysis, we can predict the outcome of the ANL mass measurements. The posterior distribution for  $\eta(\theta)^{(3)}$  for the calibrated model can be obtained by propagating the posterior draws for  $\theta$  through the ANL mass emulator. The resulting 90% intervals are given by the blue intervals in Figure 10. Predictions for the new measurements  $\eta^{(3)}(\theta) + \epsilon^{(3)}$  require the variance, or a probabilistic description about the variance of  $\epsilon^{(3)}$  - the model error for the new ANL predictions. For the predictions in Figure 10 we classified each of the ANL nuclei as spherical or deformed, and assigned the appropriate precision estimate  $\lambda_y$  obtained from the spherical and deformed nuclei accordingly. Since the first 5 nuclei are spherical, their prediction uncertainty is slightly larger as compared to the remaining 36 deformed nuclei. The resulting 90% intervals are given by the light blue lines in Figure 10.

## 4. Discussion

The purpose of this paper is to describe this Bayesian model calibration approach in detail, focusing on an example in DFT-based modeling and prediction. While we have treated this statistical analysis with care, giving careful treatment to the scientific issues, this analysis is not meant to be definitive in a scientific sense. A more scientifically focused analysis is given by McDonnell et al. in this issue.

An important feature of this analysis is the impact of additional experimental data on the analysis. The prediction for new measurements is given by  $\eta(\theta) + \epsilon$ . In general, more data reduces the uncertainty regarding the model parameters  $\theta$ , reducing the uncertainty in the calibrated model  $\eta(\theta)$ . However, it will not strongly impact the



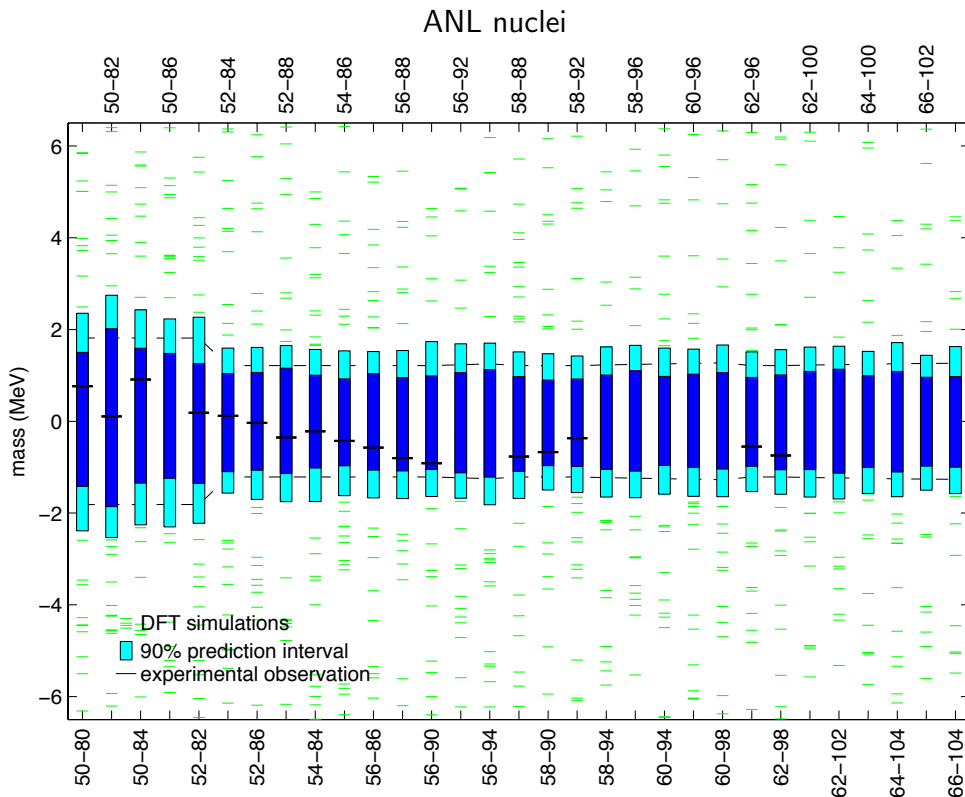


**Figure 10.** Posterior predictions for the new ANL masses. The blue intervals correspond to  $\eta(\theta)$ ; the light blue intervals correspond to  $\eta(\theta) + \epsilon$ . These predictions used only data from the 28 spherical and 47 deformed mass measurements. DFT model output is represented by the green dashes, experimental measurements by the black dashes. Each nucleus is labeled Z-N.

standard deviation of  $\epsilon$ . Hence, it is important to accurately characterize the uncertainty in the model error term  $\epsilon$  to produce realistic prediction uncertainties.

How much the uncertainty in  $\theta$  can be reduced by a particular type of data depends on the DFT model  $\eta(\cdot)$ . From Figure 7, it is clear that mass data alone will not reduce uncertainty in certain linear combinations of the model parameters. For example, moving  $1/M_s^*$  and  $C_0^{\rho\Delta\rho}$  together will not have a large impact on the DFT-computed mass. Hence the posterior uncertainty regarding these two parameters is strongly correlated. Because of this similarity in sensitivity, additional mass data will not substantially improve this situation.

This analysis estimated the error variances, allowing different precision parameters  $\lambda_y$  for the spherical and deformed masses. This results in a posterior distribution for  $\theta$  that gives more accurate results for deformed nuclei, relative to the spherical ones. In contrast, previous analyses [10, 11] have given equal weight to the two data types. There the weights  $w$  in the objective function effectively specify the precision  $\lambda_y$  for each data type ( $w = \lambda_y^{-\frac{1}{2}}$ ), leading to a different posterior distribution for  $\theta$ .

## Acknowledgment

This work was supported by the SciDAC activity within the U.S. Department of Energy, Office of Science, Advanced Scientific Computing Research program. Computational resources were provided through an INCITE award “Computational Nuclear Structure” by the National Center for Computational Sciences (NCCS) and National Institute for Computational Sciences (NICS) at Oak Ridge National Laboratory, through an award by the Livermore Computing Resource Center at Lawrence Livermore National Laboratory, and through an award by the Laboratory Computing Resource Center at Argonne National Laboratory.

## References

- [1] J. P. Kaipio and E. Somersalo. *Statistical and Computational Inverse Problems*. Springer, New York, 2004.
- [2] A. Tarantola. *Inverse problem theory and methods for model parameter estimation*. Society for Industrial Mathematics, 2005.
- [3] M. Kennedy and A. O’Hagan. Bayesian calibration of computer models (with discussion). *Journal of the Royal Statistical Society (Series B)*, 68:425–464, 2001.
- [4] J Van Schelt, D Lascar, G Savard, JA Clark, PF Bertone, S Caldwell, A Chaudhuri, AF Levand, G Li, GE Morgan, et al. First results from the caribu facility: mass measurements on the r-process path. *Physical review letters*, 111(6):061102, 2013.
- [5] D. Higdon, M. Kennedy, J. Cavendish, J. Cafoe, and R. D. Ryne. Combining field observations and simulations for calibration and prediction. *SIAM Journal of Scientific Computing*, 26:448–466, 2004.
- [6] M. J. Bayarri, J. O. Berger, R. Paulo, J. Sacks, J. A. Cafoe, J. Cavendish, C. Lin, and J. Tu. A framework for validation of computer models. *Technometrics*, 49:138–154, 2007.
- [7] Jerome Sacks, William J. Welch, Toby J. Mitchell, and Henry P. Wynn. Design and analysis of computer experiments (with discussion). *Statistical Science*, 4:409–423, 1989.
- [8] J. Oakley and A. O’Hagan. Probabilistic sensitivity analysis of complex models. *Journal of the Royal Statistical Society (Series B)*, 66:751–769, 2004.
- [9] E.N. Ben-Ari and D.M. Steinberg. Modeling data from computer experiments: an empirical comparison of kriging with mars and projection pursuit regression. *Quality Engineering*, 19(4):327–338, 2007.
- [10] Markus Kortelainen, Thomas Lesinski, J Moré, W Nazarewicz, J Sarich, N Schunck, MV Stoitsov, and S Wild. Nuclear energy density optimization. *Physical Review C*, 82(2):024313, 2010.
- [11] M Kortelainen, J McDonnell, Witold Nazarewicz, P-G Reinhard, J Sarich, N Schunck, MV Stoitsov, and SM Wild. Nuclear energy density optimization: Large deformations. *Physical Review C*, 85(2):024304, 2012.
- [12] Dani Gamerman and Hedibert F Lopes. *Markov chain Monte Carlo: stochastic simulation for Bayesian inference*. CRC Press, 2006.
- [13] William J. Welch, Robert J. Buck, Jerome Sacks, Henry P. Wynn, Toby J. Mitchell, and Max D. Morris. Screening, predicting, and computer experiments. *Technometrics*, 34:15–25, 1992.
- [14] A. O’Hagan. Bayesian analysis of computer code outputs: a tutorial. *Reliability Engineering & System Safety*, 91(10):1290–1300, 2006.
- [15] Katrin Heitmann, Dave Higdon, Salman Habib, and Charlie Nakhleh. Cosmic calibration. *Astrophysical Journal Letters*, 646:L1, 2006.
- [16] B. Sanso, C.E. Forest, and D. Zantedeschi. Inferring climate system properties using a computer model. *Bayesian Analysis*, 3(1):1–38, 2008.

- [17] Boxin Tang. Orthogonal array-based Latin hypercubes. *Journal of the American Statistical Association*, 88:1392–1397, 1993.
- [18] Thomas J. Santner, Brian J. Williams, and William I. Notz. *Design and analysis of computer experiments*. Springer, New York, 2003.
- [19] D. Higdon, J. Gattiker, B. Williams, and M. Rightley. Computer Model Calibration Using High-Dimensional Output. *Journal of the American Statistical Association*, 103(482):570–583, 2008.
- [20] J. O. Ramsay and B. W. Silverman. *Functional Data Analysis*. Springer, New York, 1997.
- [21] Hans von Storch and Francis W. Zwiers. *Statistical Analysis in Climate Research*. Cambridge University Press, New York, 1999.
- [22] J. Besag, P. J. Green, D. M. Higdon, and K. Mengersen. Bayesian computation and stochastic systems (with discussion). *Statistical Science*, 10:3–66, 1995.
- [23] N. Metropolis, A. Rosenbluth, M. Rosenbluth, A. Teller, and E. Teller. Equations of state calculations by fast computing machines. *Journal of Chemical Physics*, 21:1087–1091, 1953.
- [24] W. K. Hastings. Monte Carlo sampling methods using Markov chains and their applications. *Biometrika*, 57:97–109, 1970.
- [25] M. Kortelainen, J. McDonnell, W. Nazarewicz, P.-G. Reinhard, J. Sarich, N. Schunck, M. V. Stoitsov, and S. M. Wild. Nuclear energy density optimization: Large deformations. *Phys. Rev. C*, 85:024304, Feb 2012.